Bulletin of the Seismological Society of America, Vol. 107, No. 1, pp. –, February 2017, doi: 10.1785/0120160186

Ⓔ

Short Note

Frequency-Dependent Effects of 2D Random Velocity Heterogeneities in the Mantle Lid on *Pn* Geometric Spreading

by Xiao-Bi Xie and Thorne Lay

Abstract Geometric spreading of the *Pn* phase for shallow sources, which refracts through the uppermost mantle and is the first seismic-wave arrival at distances of ~200 to ~1500 km, is expected to be frequency dependent for most velocity structures. The smoothly varying distance and frequency dependence of *Pn* geometric spreading predicted for simple 1D spherical structures are dependent upon precise interference of multiple underside reflections from the Moho boundary. This interference is strongly impacted by lateral variations in the velocity structure. Prior work has shown that the presence of 2D random heterogeneities in the mantle lid or topography of the Moho boundary modifies *Pn* geometric spreading for ~1 Hz signals, suppressing the distinctive character of the distance dependence for a 1D structure and approaching a power-law behavior as the root mean square (rms) strength of the heterogeneity increases. Here, 2D finite-difference calculations of the effects of random heterogeneities in the mantle lid on the *Pn* geometric spreading are extended to frequencies of up to 10 Hz, quantifying the frequency dependence. Although the shape of the distance dependence is still systematically modified, the strength of the frequency dependence is actually increased from that for homogeneous models for many suites of models with varying rms perturbations and correlation lengths of exponential random heterogeneity distributions superimposed on constant and linear gradient background mantle lid velocity structures. This indicates that assumption of frequency-independent power-law spreading for *Pn* directly introduces artificial frequency dependence to inferred attenuation coefficients. Similar behavior is expected for *Sn* phases. Efforts to characterize the mantle lid heterogeneity spectrum are required to overcome this trade-off with anelasticity representations.

Electronic Supplement: Figures showing calculated *Pn*-wave spectral amplitudes versus distance.

Introduction

It is now well established that *Pn* (and *Sn*) cannot usually be treated as a simple conical headwave developed along a flat Moho discontinuity (e.g., Červený and Ravindra, 1971; Hill, 1973; Menke and Richards, 1980; Sereno and Given, 1990; Nowack and Stacy, 2002; Yang *et al.*, 2007; Yang, 2011). Figure 1 schematically depicts the main factors that affect the amplitude of *Pn*. A true headwave case is produced by a low constant-velocity crust overlying a high constant-velocity mantle with a planar Moho discontinuity (Fig. 1a). A source located in the crust will excite wave energy that propagates from the source to the refracting point at the Moho and then horizontally in the mantle immediately below the Moho. Energy of this high-speed mantle wave leaks back to the crust and can be observed as a headwave in the upper medium. The wave energy immediately below the Moho is rapidly depleted without being recharged by refractions from greater depth, and there is no characteristic scale length in this system. These result in frequency-independent strong power-law decay of the observed headwave amplitude.

Actual *Pn*-wave propagation for a spherical Earth is much more complicated, because the phase involves interference of multiple-diving waves reflected from the underside of the Moho discontinuity. Menke and Richards (1980), Sereno and Given (1990), Yang *et al.* (2007), and Avants *et al.* (2011) studied *Pn* waves in flat and spherical earth models and found that Earth's sphericity alone can cause nonheadwave and frequency dependence of *Pn* geometrical spreading. Sphericity acts similarly to a positive velocity gradient in the mantle of a flat earth

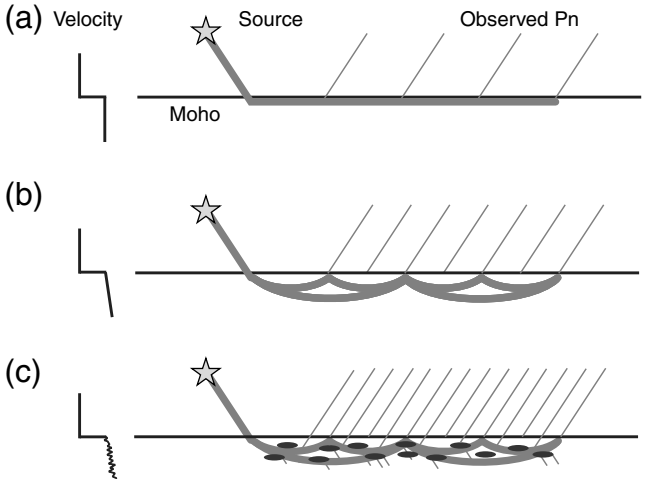

Figure 1. *Pn* waves in different crust–upper-mantle velocity models, with (a) constant velocity crust and upper mantle, and a planar Moho, giving rise to a true conical headwave; (b) vertical velocity gradient in the upper mantle, giving rise to the frequency-dependent spreading examined by Sereno and Given (1990) and Yang *et al.* (2007), and (c) laterally varying fine-scale velocity heterogeneity in the upper mantle giving rise to modified *Pn* geometric spreading as analyzed by Avants *et al.* (2011).

structure (Fig. 1b), producing a whispering gallery. This is either augmented or reduced by any actual depth variation of velocity in the mantle lid below the Moho (a negative critical velocity gradient in the mantle lid that perfectly balances the sphericity effect is required to produce a true headwave in spherical models). For a positive velocity gradient, the energy penetrating to larger depth can refract to feed the depleted energy traveling just below the Moho, making *Pn* much stronger than if it were a true headwave and actually increasing amplitudes at large distance, giving smooth concave upward amplitude–distance curves. The positive gradient provides a characteristic length scale, resulting in the frequency dependence.

Scattering from lateral velocity variations in the uppermost mantle will affect *Pn* waves differently than it affects other waves (Fig. 1c). For most body and surface waves, scattering deflects wave energy away from the main propagation direction, causing the wave amplitude to decrease. This process is known as scattering attenuation. However, *Pn*-wave energy is mainly confined to the mantle lid by the Moho discontinuity and the upper-mantle velocity gradient. In a laterally smooth waveguide, relatively little energy escapes from the main propagation channel to radiate upward to form observable *Pn*. The presence of small-scale heterogeneities in the upper mantle causes scattering with two effects on *Pn* propagation. First, as for other waves, the scattering causes progressive attenuation along the upper-mantle channel. Second, the scattering provides an efficient mechanism to increase observed *Pn* amplitude by deflecting the energy away from the main propagation direction in the upper mantle. Compared to otherwise very weak *Pn* energy, the scattered energy can cause prominent enhancement of the *Pn* amplitudes. This leads to a dilemma as to whether the scattering should be treated as scattering attenuation, or as *Pn* geometrical spreading; both are elastic effects controlled by the velocity structure. Avants *et al.* (2011) modeled the effects of heterogeneity in the Moho depth and within the mantle lid for ~1 Hz *Pn* energy, showing that the two effects of scattering tend to suppress any increase of *Pn* amplitude at large distance, causing 1-Hz geometric spreading curves to approach power-law representations, even while the overall amplitude–distance curves are shifted higher than for a headwave.

Pn in Heterogeneous Models

In this article, we extend the finite-difference calculations of Avants *et al.* (2011) to higher frequency to evaluate frequency-dependent effects of the fine-scale heterogeneities on *Pn* geometric spreading behavior. The goal is to evaluate whether the heterogeneity effects are similar to those for 1 Hz waves and whether the intrinsic frequency dependence is suppressed such that a single power-law spreading relationship for all frequencies (as commonly used) is valid. This issue is of particular importance for utilization of *Pn* amplitudes in estimation of nuclear test yields, event identification, and tomographic *Pn* attenuation models (e.g., Taylor *et al.*, 1989; Walter *et al.*, 1995; Fisk *et al.*, 2005; Xie, 2007; Zhao *et al.*, 2015).

The finite-difference method has been used for investigating *Pn*-wave propagation in models with lateral heterogeneities either in the upper mantle (e.g., Ryberg *et al.*, 2000; Avants *et al.*, 2011), or in the lower crust (Nielsen and Thybo, 2003). We perform 2D calculations using enhanced versions of the code of Xie and Lay (1994), exploiting advances in computational capacity to stably compute synthetic *Pn* with bandwidth up to 10 Hz out to distances of 1000 km, explicitly extending the bandwidth of synthetics for the models with upper-mantle heterogeneities presented by Avants *et al.* (2011). We do not address the issue of lower crustal heterogeneity, because that was not considered by Avants *et al.* (2011). High-frequency computations in 3D are still too distance limited to be useful for our goal. As in Avants *et al.* (2011), the random velocity models are generated by adding velocity and density perturbations to mantle models, keeping a constant velocity crust. Below the Moho discontinuity, the mantle has a specified vertical (radial) positive velocity gradient of 0.000, 0.001, or 0.002. Below this gradient layer, the mantle follows the IASP91 earth model (Kennett and Engdahl, 1991). The random velocity perturbations have an exponential spectrum, characterized by the horizontal and vertical correlation lengths and the root mean square (rms) velocity perturbation. Both *P*- and *S*-wave velocities have the same percentage perturbations, and the density perturbation is half of the velocity perturbation. The suites of model parameters are listed in Table 1.

For each group of random heterogeneity parameters, we generate five velocity realizations using different random seeds and calculate the wave propagation in these models to 1000 km distance. The source time function is a Gaussian derivative $(t - t_s)\exp[-(t - t_s)^2/\tau^2]$, with $\tau = 0.2$ s. The earth flattening transform is used to convert the spherical model into a flat-earth model. We apply the appropriate correction of a

Table 1
2D Velocity Models with Fine-Scale Heterogeneity

Number	Background Model	Type of Random Function	Correlation Lengths (Horizontal × Vertical)	rms Perturbation (%)	Random Seeds Used
1	Const lid (0.000)	Exponential	20 km × 6 km	0.5	3,5,7,8,9
2	Const lid (0.000)	Exponential	20 km × 6 km	1.0	3,5,7,8,9
3	Const lid (0.000)	Exponential	20 km × 6 km	2.0	3,5,7,8,9
4	Const lid + 0.001 grad.	Exponential	20 km × 6 km	0.5	3,5,7,8,9
5	Const lid + 0.001 grad.	Exponential	20 km × 6 km	1.0	3,5,7,8,9
6	Const lid + 0.002 grad.	Exponential	20 km × 6 km	1.0	3,5,7,8,9
7	Const lid + 0.001 grad.	Exponential	40 km × 10 km	0.5	3,5,7,8,9
8	Const lid + 0.001 grad.	Exponential	40 km × 10 km	1.0	3,5,7,8,9
9	Const lid + 0.001 grad.	Exponential	10 km × 3 km	1.0	3,5,7,8,9

Const lid, constant velocity mantle lid; grad., velocity gradient; rms, root mean square.

factor of $1/\sqrt{r}$, in which r is the epicentral distance, to map our 2D line sources into 3D spherical sources (e.g., Avants *et al.*, 2011). Figure 2 shows snapshots of wavefields propagating in structures without and with random velocity fluctuations. Figure 2a,b shows the wavefield in the background velocity model, and Figure 2c,d shows the wavefield in a velocity model with 1% rms velocity perturbations below the Moho. The pervasive generation of scattered waves is readily evident in the snapshots, particularly in the leading wave (*Pn*) coda.

The synthetic seismograms are processed using the following procedure:

1. narrow bandpass filter the seismograms with central frequencies 0.4, 0.8, 1.5, 3.0, 6.0, and 10.0 Hz;
2. group velocity window between 8.2 and 7.6 km/s to isolate the *Pn* signal;
3. calculate the rms amplitude within the group velocity window;
4. normalize all of the amplitudes by the spectral levels from the corresponding 1D velocity model calculations at a reference distance of 300 km; and
5. calculate the mean value from five realizations of the random structure.

Figure 3 presents calculations of the *Pn*-wave spectral amplitudes versus distance for random velocity model 1 listed in Table 1. Figure 3a–f is for frequencies 0.4, 0.8, 1.5, 3.0, 6.0, and 10.0 Hz, respectively. Light-colored symbols are amplitudes calculated from individual random realizations. Solid squares with error bars are mean values and standard deviations from the five realizations. The solid diamonds are from the background 1D velocity model. The normalization of amplitudes relative to the background model at a reference distance of 300 km accounts for the effects of the source spectrum and filter passband. To facilitate comparison, Figure 3g compiles the decay curves for different frequencies in the 1D background model. These are smooth, frequency-dependent concave-upward curves with an amplitude minimum typical of all simple spherical models (Yang *et al.*, 2007; Avants *et al.*, 2011). Figure 3h shows the related average decay curves in the models with random velocity perturbations. The amplitudes are systematically larger than for the homogeneous models, and the curves have less well-defined minima. Moreover, they also have enhanced overall frequency-dependent variation relative to the background model. Corresponding and qualitatively very similar behavior for the other eight models in Table 1 are shown in Ⓔ Figures S1–S8 (available in the electronic supplement to this article).

A summary of the mean model behavior for all nine models in Table 1 is provided in Figure 4. Figure 4a–i corresponds to models 1–9, respectively. Red symbols indicate the frequency-dependent amplitude behavior for the homogeneous reference model for each case. For each model, the *Pn* amplitudes for the heterogeneous structure are enhanced relative to the 1D reference structure underlying the heterogeneity. This is a direct manifestation of the dominant effect of scattering of strong energy out of the lid waveguide into the crustal *Pn* phase as depicted in Figure 1c and captured in the snapshot in Figure 2c,d. The effect increases with frequency, keeping in mind that the spectral levels are relative to the reference distance of 300 km where the structural effects and scattering effects are relatively minor. The random models have variability as seen in Figure 3 and in Ⓔ Figures S1–S8, but the average behavior over the five realizations tends to be quite stable. Some of the small-scale structure in the amplitude curves may begin to average out with a greater number of realizations, but some of it is likely to persist as a manifestation of the specific fabric of the heterogeneity spectrum. Although smooth curvature of the patterns and the increase with distance for the stronger gradient background models is suppressed in the scattering calculations, the overall frequency dependence of the models is actually enhanced in all cases relative to the 1D reference case.

The following features are revealed:

1. When the upper-mantle velocity gradient is small (the 0.000 case limits it to only the sphericity-caused gradient), scattering dominates the process that boosts the *Pn* amplitude.
2. At low frequencies, the scattering effect is weak. For example, at 0.4 Hz, scattering has very weak contribution.
3. The scattering effect is proportional to the rms of the heterogeneity.
4. The weakest effects are seen for 0.4 Hz and rms = 0.5%. Under this circumstance, the scattering has little contribution to the *Pn* amplitude.

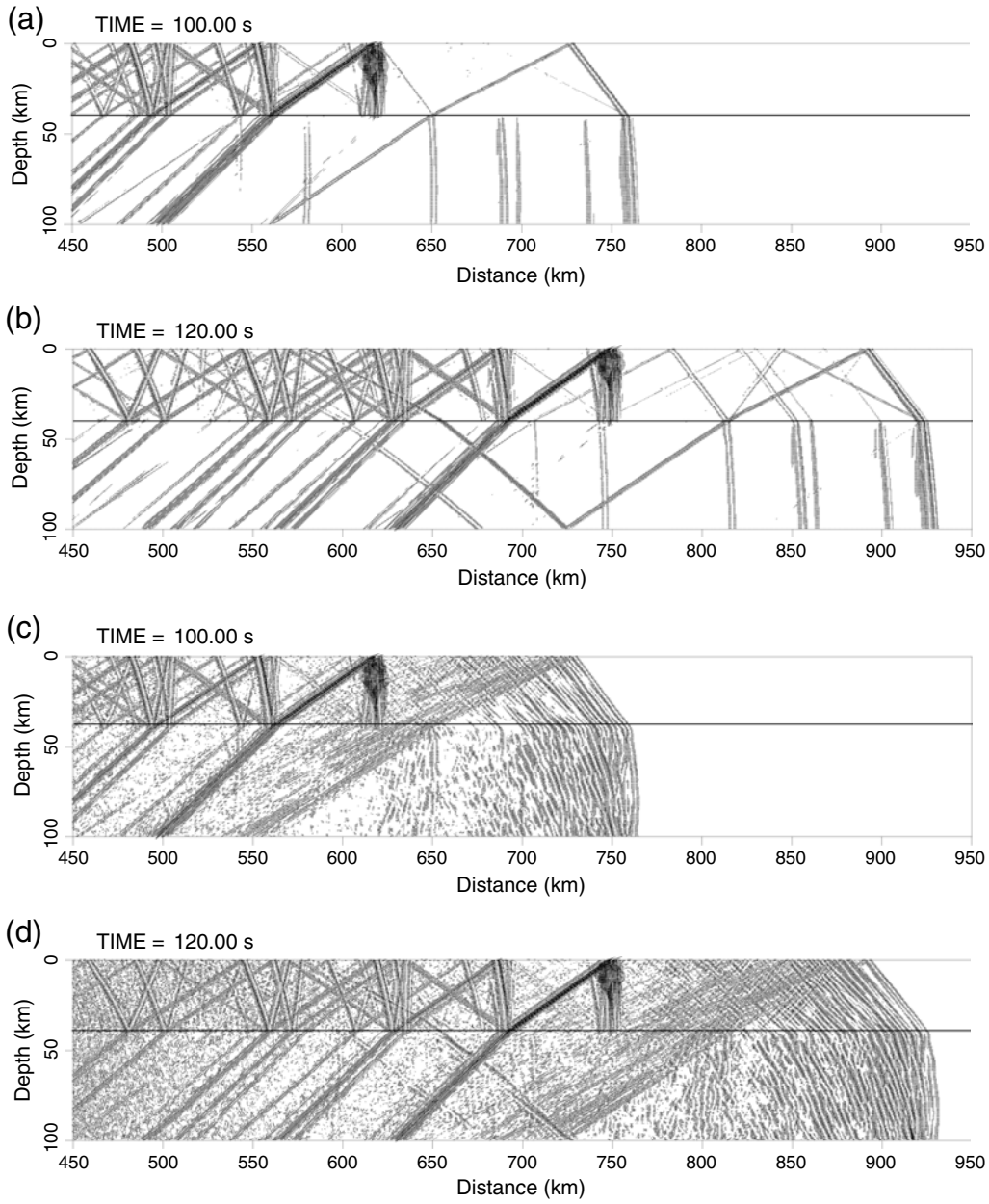

Figure 2. (a,b) Wavefield snapshots in a homogeneous velocity model and (c,d) a model with small-scale random velocity perturbations in the mantle. The background model for both cases has a 40-km-thick constant velocity crust and an upper mantle with 0.001 vertical velocity gradient. The upper mantle for the calculations in (c) and (d) has 1% root mean square (rms) velocity perturbations and the horizontal and vertical correlations lengths are 20 and 6 km, respectively. *Pn* is the leading arrival.

5. In models with medium-to-large upper-mantle velocity gradient, scattering strongly affects the *Pn* amplitude at short distances. However, at large distances, the effect of scattering to *Pn* amplitude is diminished. This is because the cumulative strong scattering attenuates the energy in the upper-mantle waveguide. A larger velocity gradient tends to deflect more energy out of the waveguide progressively, so the amplitudes do not increase as much with distance in a relative sense as they do for the homogeneous models.
6. In all cases, scattering tends to quasi-linearize the average *Pn* amplitude decay curves, shifting them from quadratic to linear (power law) in log–log coordinates, but the curves clearly do not converge to a single frequency-independent level.

These calculations reaffirm that the 1 Hz calculations of Avants *et al.* (2011) capture some of the basic effect of the heterogeneous structure, but for the first time we find that the intrinsic frequency dependence is not lost as a result of the scattering. The actual small-scale structure on any given path in the Earth is not known, but the reasonable inference by some researchers examining the earlier 1 Hz calculations that such scattering will homogenize the signals to an extent that no overall

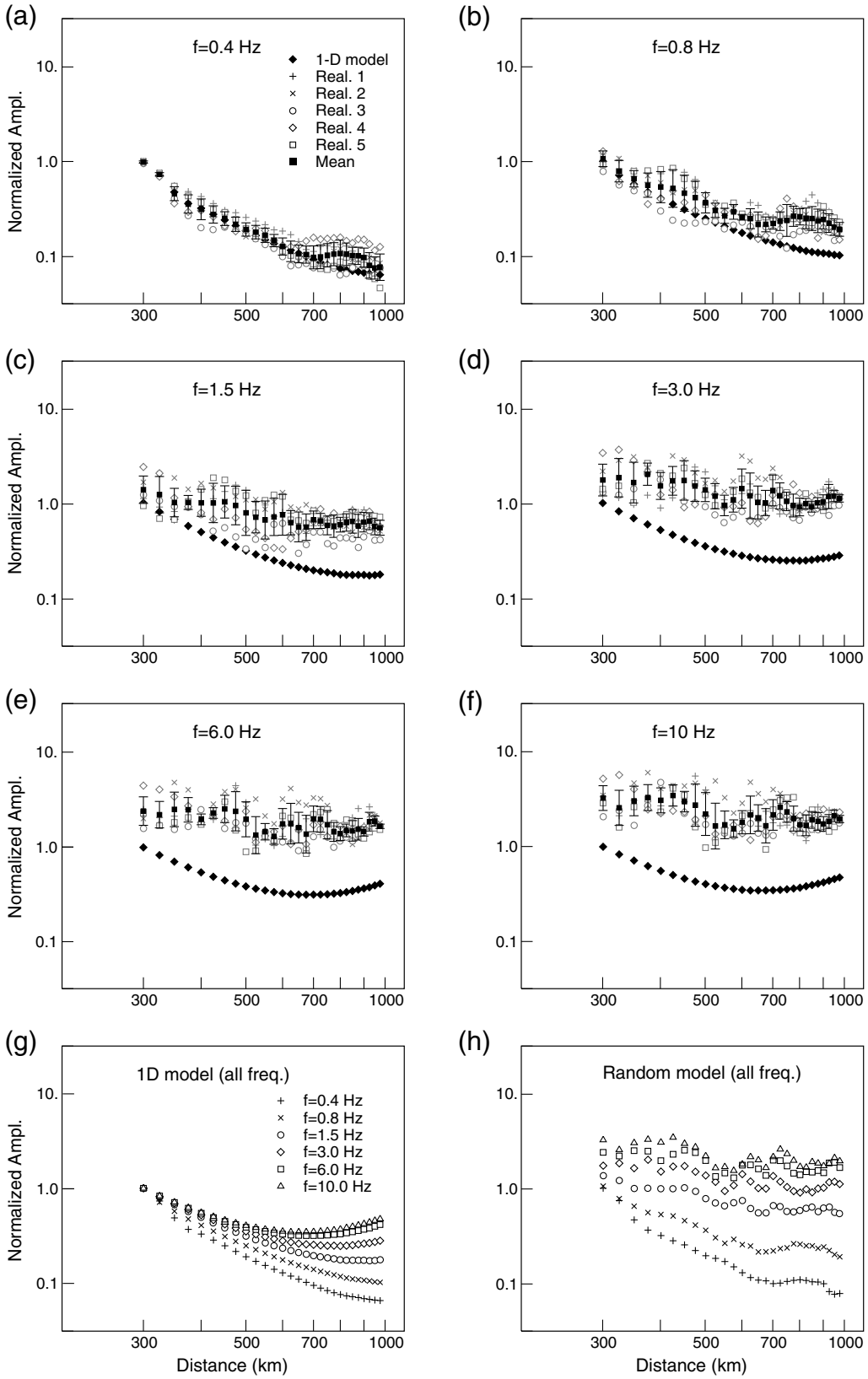

Figure 3. *Pn*-wave spectral amplitude versus distance calculated from the random velocity model 1 in Table 1. Spectral amplitudes at frequencies (a) 0.4, (b) 0.8, (c) 1.5, (d) 3.0, (e) 6, and (f) 10 Hz. Different symbols correspond to different realizations. (g) Amplitudes in the 1D background model. Different symbols indicate frequency. (h) Mean amplitudes for the random velocity model.

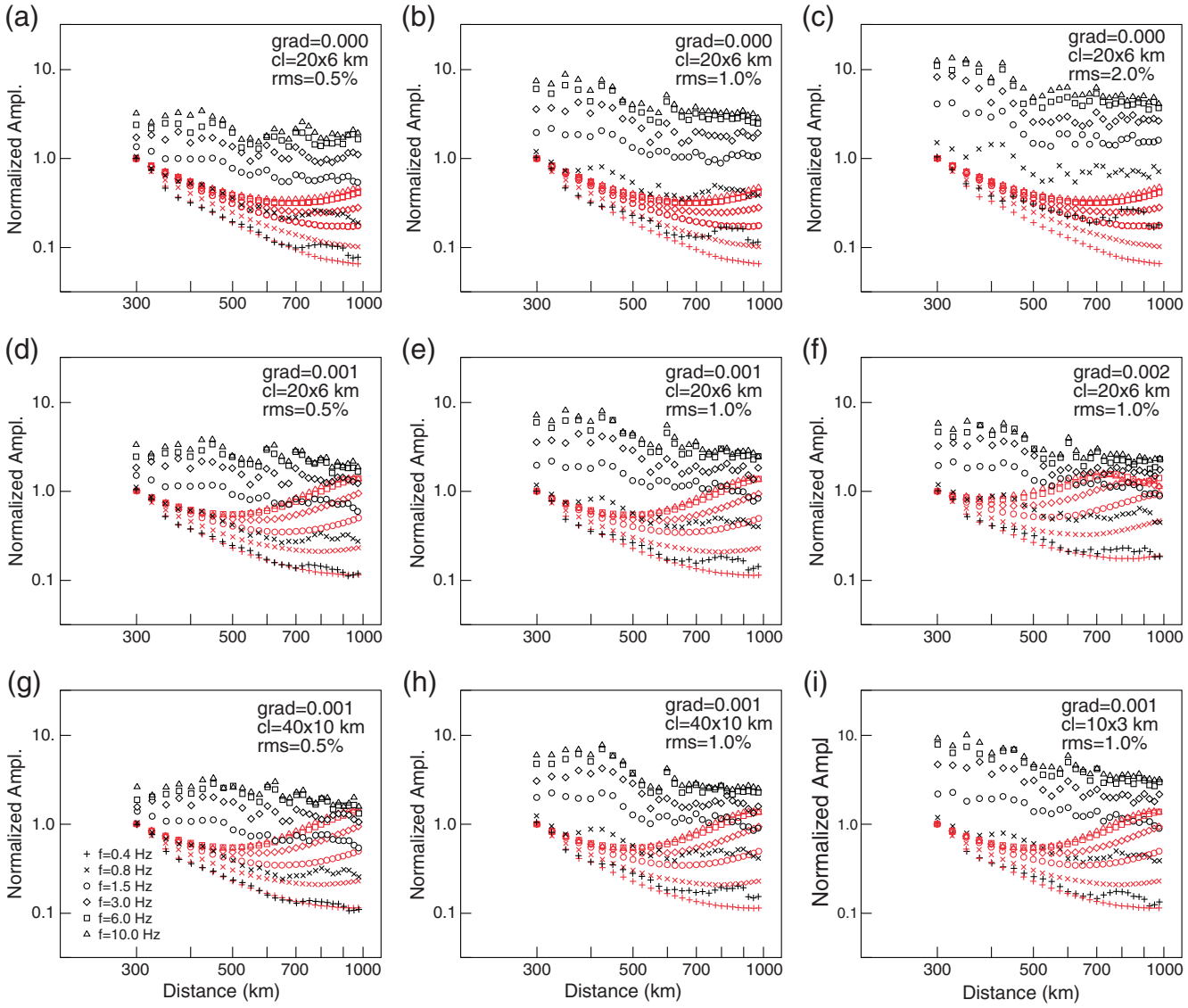

Figure 4. *Pn* amplitude-decay curves for velocity models with (black symbols) and without (red symbols) upper-mantle velocity perturbations. Panels (a–i) are for velocity models 1–9 with parameters listed in Table 1, with parameters background mantle velocity gradient (grad), correlation length (cl), and rms strength (rms) labeled in each panel. Symbols for different frequencies are indicated in (*g*).

frequency dependence of the *Pn* spreading will be manifested, allowing use of a single frequency-independent power-law decay relationship, is clearly not supported by these calculations.

The suite of calculations in Figure 4 can be evaluated in detail for the dependence on rms velocity perturbation strength for a given reference structure and correlation length (e.g., Ⓔ Fig. S9). Increasing the rms causes prominent amplitude increase, with high-frequency signals being more sensitive to the scattering. Varying the strength of the background velocity gradient for a fixed correlation length and rms perturbation heterogeneity model reveals (e.g., Ⓔ Fig. S10) that in the presence of small-scale heterogeneities in the mantle, the scattering effect dominates, and the decay curves become less sensitive to the upper-mantle velocity gradient. This may partially relax the requirement of determining accurate upper-mantle velocity gradients when measuring *Pn* attenuation. The decay curves tend to approach a power-law behavior due to the deflection of more energy from the upper mantle into the crust, raising the concave part of the decay curve at intermediate distance, whereas the large distances are reduced by the net scattering attenuation. The combined effect makes a more uniform rate of decay, but it is not approaching the frequency-independent behavior found for a conical headwave. One can also consider suites of random velocity models having the same upper-mantle velocity gradients and the same rms velocity perturbation but different horizontal and vertical correlation lengths (e.g., Ⓔ Fig. S11). Within the investigated frequency band, *Pn* is found to be only weakly dependent on the size and aspect ratios of the heterogeneities. Perturbations with horizontal and vertical correlation lengths of 10 and 3 km cause the most scattering of the models considered.

Discussion and Conclusions

New 2D computations of *Pn* geometric spreading in media with small-scale heterogeneities in the uppermost mantle extend the work of Avants *et al.* (2011) from near 1 Hz to out to 10 Hz at 1000-km propagation distance. All calculations, for suites of heterogeneity realizations, indicate some modification of the amplitude–distance trends for *Pn*, but the intrinsic frequency dependence of models with radial velocity gradients is systematically enhanced by the presence of small-scale lithospheric heterogeneity. This is the result of scattering of *Pn* energy out of the lid waveguide into the crust. Although the general trends of the amplitude distance terms for each frequency do tend to approach the commonly assumed power-law decay form, there is associated enhanced frequency dependence, which is not commonly assumed or recognized. This further weakens the rationale for using frequency-independent power-law representations of *Pn* (and *Sn*) geometric spreading. Given that the only spherical earth structures that will result in frequency-independent power-law behavior are homogeneous models with negative critical gradients in the mantle lid (a possible but probably very rare situation), we endorse the contention of Yang (2011) that a basic velocity model-based frequency-dependent correction, or an empirically/theoretically grounded correction, is a more sensible choice than a frequency-independent power-law geometric spreading to use in *Pn* and *Sn* analysis. By focusing on extending the results of Avants *et al.* (2011), we have not addressed the effects of fine-scale lower crustal heterogeneity, which can also contribute to *Pn* complexity (e.g., Nielsen and Thybo, 2003), but it is likely that similar behavior will occur for such models.

Currently, there are few data that constrain actual crustal and uppermost mantle small-scale heterogeneity parameters (e.g., lid velocity gradient, and power spectrum and rms perturbation of the velocities and density). Therefore, very general velocity models are adopted in our simulations. Because of computational limitations, 2D models are used; 3D scattering may add further complexity. Although any specific path will have unique large- and small-scale structural features, the general influence of the small-scale heterogeneities on *Pn* spreading is likely to be similar to the behavior shown here. Efforts to determine frequency-dependent attenuation maps for *Pn* and *Sn* will be directly affected by the choices made for elastic geometric spreading behavior, and given the lack of specific knowledge of fine-scale structure on each path, there is an intrinsic trade-off between frequency-dependent attenuation and geometric spreading that must be recognized to avoid overinterpretation of inferred attenuation models. Improving the characterization of the heterogeneity spectrum is the only way to overcome this trade-off.

Data and Resources

All the data used in this article are computer generated calculations.

Acknowledgments

We appreciate discussions with X. (David) Yang during this analysis. We thank an anonymous reviewer for thoughtful comments on the article. This work was supported by the Air Force Research Laboratory under Contract Number FA9453-12-C-0234.

References

Avants, M., T. Lay, X.-B. Xie, and X. Yang (2011). Effects of 2D random velocity heterogeneities in the mantle lid and Moho topography on *Pn* geometric spreading, *Bull. Seismol. Soc. Am.* **101,** 126–140.

Červený, V., and R. Ravindra (1971). *Theory of Seismic Head Waves*, University of Toronto Press, Toronto, Ontario.

Fisk, M. D., S. R. Taylor, and T. Lay (2005). Modeling and empirical research on energy partitioning of regional seismic phases used for explosion monitoring, *Proc. of the 27th Seismic Research Review*, 539–549.

Hill, D. P. (1973). Critically refracted waves in a spherically symmetric radially heterogeneous Earth model, *Geophys. J. Roy. Astron. Soc.* **34,** 149–177.

Kennett, B. L. N., and E. R. Engdahl (1991). Traveltimes for global earthquake location and phase identification, *Geophys. J. Int.* **105,** no. 2, 429–465, doi: 10.1111/j.1365-246X.1991.tb06724.x.

Menke, W. H., and P. G. Richards (1980). Crust-mantle whispering gallery phases: A deterministic model of teleseismic Pn wave propagation, *J. Geophys. Res.* **85,** no. B10, 5416–5422.

Nielsen, L., and H. Thybo (2003). The origin of teleseismic Pn waves: Multiple crustal scattering of upper mantle whispering gallery phases, *J. Geophys. Res.* **108,** no. B10, 2460, doi: 10.1029/2003JB002487.

Nowack, R. L., and S. M. Stacy (2002). Synthetic seismograms and wide-angle seismic attributes from the Gaussian beam and reflectivity methods for models with interfaces and velocity gradients, *Pure Appl. Geophys.* **159,** 1447–1464.

Ryberg, T., M. Tittgemeyer, and F. Wenzel (2000). Finite difference modeling of *P*-wave scattering in the upper mantle, *Geophys. J. Int.* **141,** 787–800.

Sereno, T. J., and J. W. Given (1990). *Pn* attenuation for a spherically symmetric Earth model, *Geophys. Res. Lett.* **17,** 1141–1144.

Taylor, S. R., M. D. Denny, E. S. Vergino, and R. E. Glaser (1989). Regional discrimination between NTS explosions and western U.S. earthquakes, *Bull. Seismol. Soc. Am.* **79,** 1142–1176.

Walter, W. R., K. M. Mayeda, and H. Patton (1995). Phase and spectral ratio discrimination between NTS earthquakes and explosions. Part I: Empirical observations, *Bull. Seismol. Soc. Am.* **85,** 1050–1067.

Xie, J. (2007). *Pn* attenuation beneath the Tibetan plateau, *Bull. Seismol. Soc. Am.* **84,** 2040–2052, doi: 10.1785/0120070016.

Xie, X. B., and T. Lay (1994). The excitation of *Lg* waves by explosions: A finite-difference investigation, *Bull. Seismol. Soc. Am.* **84,** 324–342.

Yang, X. (2011). A *Pn* spreading model constrained with observed amplitudes in Asia, *Bull. Seismol. Soc. Am.* **101,** 2201–2211, doi: 10.1785/0120100314.

Yang, X., T. Lay, X. Xie, and M. S. Thorne (2007). Geometric spreading of *Pn* and *Sn* in a spherical Earth model, *Bull. Seismol. Soc. Am.* **97,** 2053–2065.

Zhao, L.-F., X.-B. Xie, B.-F. Tian, Q.-F. Chen, T.-Y. Hao, and Z.-X. Yao (2015). *Pn*-wave geometrical spreading and attenuation in northeast China and the Korean peninsula constrained by observations from North Korean nuclear explosions, *J. Geophys. Res.* **120,** no. 11, 7558–7571, doi: 10.1002/2015JB012205.

Department of Earth and Planetary Sciences
University of California Santa Cruz
1156 High Street
Santa Cruz, California 95064
tlay@ucsc.edu

Manuscript received 10 June 2016;
Published Online 15 November 2016